Journal of Power Sources 472 (2020) 228334

Contents lists available at ScienceDirect

Journal of Power Sources

journal homepage: www.elsevier.com/locate/jpowsour

Real-time visualization of Zn metal plating/stripping in aqueous batteries with high areal capacities

Sechan Lee [a,f,1], Inyeong Kang [a,b,f,1], Jihyeon Kim [a], So hee Kim [d], Kisuk Kang [a,d,e,f,**], Jihyun Hong [c,*]

[a] Department of Materials Science and Engineering, Seoul National University, 1 Gwanak-ro, Gwanak-gu, Seoul, 08826, Republic of Korea
[b] Research Institute of Advanced Materials (RIAM), Seoul National University, 1 Gwanak-ro, Gwanak-gu, Seoul, 08826, Republic of Korea
[c] Center for Energy Materials Research, Korea Institute of Science and Technology (KIST), 14 Gil 5 Hwarang-ro, Seongbuk-gu, Seoul, 02792, Republic of Korea
[d] Advanced Analysis Center, Korea Institute of Science and Technology (KIST), 14 Gil 5 Hwarang-ro, Seongbuk-gu, Seoul, 02792, Republic of Korea
[e] Center for Nanoparticle Research, Institute for Basic Science (IBS), Seoul National University, 1 Gwanak-ro, Gwanak-gu, Seoul, 08826, Republic of Korea
[f] Institute of Engineering Research, College of Engineering, Seoul National University, 1 Gwanak-ro, Gwanak-gu, Seoul, 08826, Republic of Korea

HIGHLIGHTS

- *Operando* optical microscopic observation of Zn plating/stripping is demonstrated.
- Correlation between electrolyte and microstructure of Zn metal is established.
- Denser Zn agglomerates with finer Zn particles enables the better cyclability.
- Stable SEI layer plays a key role for reversible deposition/stripping of Zn.

GRAPHICAL ABSTRACT

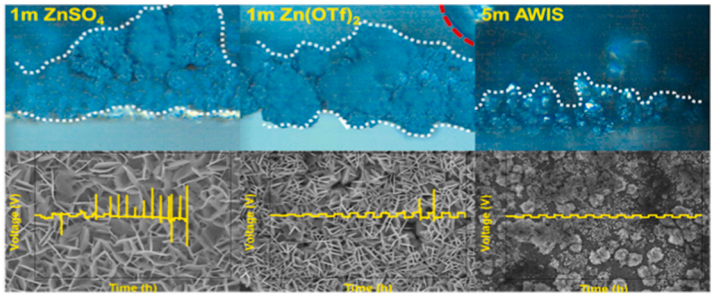

ARTICLE INFO

Keywords:
Zn aqueous batteries
Operando optical microscopy
Zn dendrites
SEI layer formation

ABSTRACT

Zinc aqueous batteries have attracted great attention due to the earth abundance and the low redox potential of Zn metal. Utilizing Zn metal as an anode, however, causes low coulombic efficiency stemming from a dendritic Zn plating and formation of byproducts such as hydrogen gas, solid zinc hydroxide and salt-related compounds. One effective way of mitigating the issues is to modify the solvation structure of the electrolyte to increase the energy barrier of the water molecules for hydrolysis and electrolysis. Nevertheless, Zn aqueous batteries still indiscriminately utilize several types of electrolytes without elucidating the correlation between electrolyte composition and the electrochemistry of Zn metal. Here, we use *operando* optical microscopy to visualize the microstructural evolution of Zn metal, which strongly affects the electrochemical reversibility. In $ZnSO_4$ electrolyte, large Zn platelets grow and form loose agglomerates vulnerable to unexpected delamination from the electrodes. In $Zn(OTf)_2$ electrolyte, Zn platelets nucleate more homogeneously and grow smaller, which forms denser agglomerates enabling more stable cycling. We further reveal that the formation of a stable solid-electrolyte interphase layer holds the key to the excellent performance of acetonitrile-hybrid water-in-salt

* Corresponding author.
** Corresponding author. Department of Materials Science and Engineering, Seoul National University, 1 Gwanak-ro, Gwanak-gu, Seoul, 08826, Republic of Korea.
E-mail addresses: matlgen1@snu.ac.kr (K. Kang), jihyunh@kist.re.kr (J. Hong).
[1] These authors contributed equally to this work.

https://doi.org/10.1016/j.jpowsour.2020.228334
Received 1 February 2020; Received in revised form 6 May 2020; Accepted 8 May 2020
Available online 19 July 2020

electrolytes. Our results show the necessity of designing proper electrolytes to develop long-life Zn aqueous batteries.

1. Introduction

Zinc (Zn) has been considered the most suitable anode material in aqueous batteries due to its high theoretical capacity (820 mAh g^{-1}), low potential (−0.762 V *vs.* SHE [standard hydrogen electrode]) that is close to the hydrogen evolution potential in basic solutions, and high abundance [1–3]. However, there is a concern that the irreversibility of Zn metal anodes may result in a low coulombic efficiency (CE). Many researchers have revealed that this irreversibility originates from the dendritic growth of Zn metal and the formation of side products, which has been almost universally observed in electrolytes with any pH values [3–7]. Alkaline electrolytes with low enough hydrogen evolution potentials produce zinc hydroxides, $Zn(OH)_2$, through the reaction between Zn and hydroxyl ions (OH^-) from hydrolysis. This reaction eventually transforms these ions into electrochemically inactive zinc oxides (ZnO), which passivate the metal surface [1,4–6,8]. Mildly acidic and near-neutral electrolytes are capable of mitigating the formation of solid side products. In these electrolytes, however, parasitic hydrogen gas evolution vigorously occurs during plating/stripping, which results in a poor cycle performance [9–12]. Once hydrogen gas evolves, the proton concentration in the electrolyte decreases, increasing the pH value above 7. This again promotes the formation of solid byproducts. Thus, regardless of the initial pH values of the electrolyte, it is difficult to avoid the series of side reactions of hydrogen evolution and the irreversible formation of byproducts [7].

The reactivity of water molecules, which is influenced by the chemical environment, is a key determinant of these side reactions [1, 13]. In dilute aqueous solutions, Zn^{2+} ions that are solvated with water molecules, (*i.e.*, Zn aqua ions; $[Zn(OH_2)_6]^{2+}$), prevail where the O–H bond of the surrounding water molecules weakens due to the interaction between the Zn^{2+} ions and the water molecules. The weak O–H bonds easily participate in hydrolysis, resulting in the formation of hydroxyl ions and triggering a zinc hydroxide formation reaction. To improve the reversibility of Zn metal in aqueous batteries, therefore, recent studies have focused more on the modification of electrolyte solvation structures to alter the bonding nature of water molecules, so that it has higher energy barriers against hydrolysis and electrolysis [1,13,14]. One effective way of doing so is to increase the concentration of salt in the electrolyte to an extreme level. This results in so-called water-in-salt electrolytes (WiSE), in which the salt ions become dominant species over the water molecules [1,13,15–17]. In this highly concentrated solution, the salt anions coordinate a Zn^{2+} cation, forming a $Zn(anion)_n$ cluster as the solvation-sheath structure. The water molecules in WiSE do not solvate the Zn^{2+} cation, thereby inhibiting hydrolysis and the accompanied formation of byproducts. Another important factor that determines the electrochemical reversibility of the metal anode in batteries is microstructural evolution during battery cycling (*e.g.*, the formation of dendritic or needle-like metal particles, which causes the internal short-circuiting or isolation of dead metal particles) [18,19]. The microstructures of metal deposits significantly vary with many properties of electrolytes, such as solvation structure, transference number, and ionic conductivity [20–22]. As such, recent scientific efforts to improve the stability of the metal anodes in batteries have been made to highlight the importance of employing appropriate electrolytes to enhance the cycle life of various rechargeable battery systems [23–25].

While the number of publications about cathode materials for Zn aqueous batteries have rapidly increased over the last few years, studies of Zn aqueous batteries still indiscriminately utilize several types of electrolytes without considering the correlation between electrolyte composition and the electrochemistry of Zn metal [26–31]. This might be attributed to the fact that studies of Zn aqueous batteries use only a small portion of Zn metal anodes in the range of a few hundred μAh cm^{-2} to a few mAh cm^{-2} of areal capacity [7,14,32,33]. Zn ions can be supplied during long-term cycling from the undamaged part of a Zn metal anode, if only a small portion of the Zn metal anode is utilized in the plating/stripping steps. Therefore, it is possible to conceal the irreversible degradation of Zn metal anodes, which limits our understanding of the reversibility of Zn metal anodes. It is necessary to comprehend the stability of Zn metal according to the types of electrolytes, even in the condition of extremely high areal capacities exceeding 10 mAh cm^{-2}, which is reasonable for practical applications.

Herein, we investigate the reversibility of the Zn metal electroplating/stripping process under high areal capacity conditions using three representative electrolytes that are widely used in Zn aqueous batteries: 1 mol kg^{-1}_{water} zinc sulfate ($ZnSO_4$) [34–37], 1 mol kg^{-1}_{water} zinc triflate ($Zn(CF_3SO_3)_2$; $Zn(OTf)_2$) [38–40], and 5 mol $kg^{-1}_{solvent}$ acetonitrile/water-in-salt (1 mol kg^{-1}_{water} $Zn(TFSI)_2$ + 20 mol kg^{-1}_{water} LiTFSI in water + acetonitrile; AWIS) [41]. Note that molality (mol $kg^{-1}{}_{solvent}$, hereafter m is used for simplicity), the number of moles of solute per kilogram of solvent, is used rather than molarity (mol $L^{-1}_{solution}$) to precisely describe the composition of the electrolytes. Titanium (Ti) foil was utilized as the substrate of the electroplating/stripping of Zn since it is widely used in the field of Zn aqueous batteries [13,16,17,32, 42–49]. Harshly deep discharge and charge processes show the impropriety of a 1 m $ZnSO_4$ solution, the reasonable stability of a 1 m $Zn(OTf)_2$ solution, and the excellent stability of a 5 m AWIS solution as electrolytes for Zn aqueous batteries. Using a combination of *operando* optical microscopy (OM) and scanning electron microscopy (SEM), we reveal that the loose agglomerates, which are composed of the coarse Zn platelets in $ZnSO_4$ electrolyte that introduce the heterogeneous delamination of the agglomerated deposits from the electrode, deteriorate the electrochemical reversibility. Denser agglomerates composed of finer platelets that form in 1 m $Zn(OTf)_2$ enhance the physical endurance of the deposits, which results in a better cycle stability. In 5 m AWIS, a gradual increase and decrease of the deposit volume was repeatedly observed with the finest Zn particles, and this secures electrochemical stability. Using X-ray photoelectron spectroscopy (XPS), we further reveal that the solid-electrolyte interphase (SEI) layer forms in electrolytes with fluorinated salts, which may enhance the adhesion strength of the Zn deposit to the Ti surface, improving the electrochemical reversibility. Our results highlight the importance of selecting proper electrolytes to investigate the intrinsic properties of novel electrode materials for higher-energy and longer-life Zn aqueous batteries. Given the correlation between the electrolyte composition, microstructure, surface (chemical) structure, and electrochemistry of Zn metal demonstrated here, the microstructural control of Zn metal in designed electrolytes and electrochemical protocols will be an interesting avenue for further study.

2. Methods

2.1. Preparation of materials

$ZnSO_4$, $Zn(CF_3SO_3)_2$ ($Zn(OTf)_2$), $LiN(CF_3SO_3)_2$ (LiTFSI), and CH_3CN (acetonitrile) were purchased from Sigma-Aldrich (UK), and Zn $((CF_3SO_3)_2N)_2$ ($Zn(TFSI)_2$) was purchased from Tokyo Chemical Industry (Japan). All the commercially available chemicals were utilized without further purification. The electrolytes (1 m $ZnSO_4$ and 1 m Zn $(OTf)_2$) were prepared by dissolving $ZnSO_4$ and $Zn(OTf)_2$ in water with the specified molality. We then prepared the 5 m AWIS electrolyte by dissolving $Zn(TFSI)_2$ and LiTFSI in water + acetonitrile with the following composition: $Zn(TFSI)_2$: 0.002 mol, 1.251 g; LiTFSI: 0.04 mol,

11.48 g; H_2O: 2 g; acetonitrile: 6.4 g [41]. Zn foil (0.25 mm thick) was purchased from Alfa Aesar (USA), and Ti foil (0.127 mm thick) was purchased from Sigma-Aldrich (UK) and used without pretreatment.

2.2. Electrochemical measurements

The voltage-time profiles of the Zn||Ti asymmetric coin-type cells (CR 2032, Wellcos Corp. Korea) were obtained. The Zn||Ti asymmetric cells were composed of a Ti working electrode (diameter: 0.375 in.) and a Zn counter/reference electrode (diameter: 0.5 in.) with a disc shape. The Celgard membrane (Celgard 3501, Wellcos Corp. Korea) was used as a separator in the coin-type cells. The electrolytes used were 1 m $ZnSO_4$, 1 m $Zn(OTf)_2$, and 5 m AWIS, and the cells were assembled in an oxygen-free atmosphere within an argon-filled glove box. The electrochemical measurements of the coin-type cells were performed at a constant current density of 5 mA cm^{-2} using a battery test system (Won-A Tech, Korea). Linear sweep voltammetry (LSV) was performed using a three-electrode beaker cell composed of a Ti working electrode (exposed area of 1 cm^2), a Zn counter electrode, and a Zn reference electrode. The voltage between the working electrode and the reference electrode was swept from the open circuit voltage to −1.0 V with a scan rate of −5 mV s^{-1}.

2.3. Operando optical microscopy (OM)

We built the *in situ* cell setup for the *operando* OM measurement by ourselves (photographs are shown in Fig. S1.). The Ti and Zn foils were used as the working and counter/reference electrodes, respectively. They were inserted into cuvettes filled with each of the three electrolytes (1 m $ZnSO_4$, 1 m $Zn(OTf)_2$, and 5 m AWIS) composing a Zn||Ti asymmetric cell. The electrochemical measurements of the *in situ* cell were performed at a constant current density of 5 mA cm^{-2} using a battery test system (Won-A Tech, Korea). The transparent side of the cuvette faced an OM object lens at a distance of 4–5 cm, and the lamp in the glove box acted as a light source. Videos of the Zn plating/stripping on the Ti foil surface were recorded with the digital camera-included OM (Nikon, LV150 N, Japan). The applied magnification of OM was 10, and the provided video in the Supplementary Information was regenerated with a 200x faster playback speed. Each snapshot obtained from the videos was captured through software provided by Microsoft, and the written accumulated capacity displayed on the bottom-right side was calculated from the obtained voltage-time profiles.

2.4. Ex situ electrode characterization

The electrodes of the Ti foil at different stages of cycling were prepared by disassembling the coin cells (rested [24 h], after the first plating step, after the first stripping step, after the second plating step, and long-term cycling [24 h]), and this was followed by rinsing the Ti electrodes with distilled water. The surface morphologies of the Ti electrodes were examined using SEM (SEM, Regulus 8230, Hitachi, Japan) equipped with an EDS (EDS, Ultim Max, Oxford, UK) attachment. The electrodes were transferred from the glove box to the SEM chamber using an air-free transfer vessel to prevent air contamination. The XPS measurements were performed in an UHV multipurpose surface analysis system (SIGMA PROBE, Thermo, UK) that operated at base pressures of $<$ 9–10 mbar. The photoelectron spectra were excited by an Al Kα (1486.6 eV) anode that operated at a constant power of 100 W (15 kV and 10 mA). All the measuring spectra were set to the reference of C 1s (284.5 eV), which correlates to the C–C bond.

3. Results and discussion

The reversibility of Zn electroplating/stripping behaviors was first electrochemically tested in three representative electrolytes that are widely used in studies of Zn aqueous batteries: 1 m zinc sulfate ($ZnSO_4$) [34–37], 1 m zinc triflate ($Zn(CF_3SO_3)_2$ or $Zn(OTf)_2$) [38–40], and 5 m AWIS (1 m $Zn(TFSI)_2$/20 m LiTFSI in water + acetonitrile) [41]. Coin cells composed of a Ti working electrode and a Zn counter/reference electrode were galvanostatically cycled at a current density of 5 mA cm^{-2} with high areal capacities of 20, 10, and 1 mAh cm^{-2}. This corresponded to 27.0%, 13.5%, and 1.35% utilizations of the Zn counter electrode, respectively. After the first deposition, successive stripping and plating were performed to use 90% of the initial capacities (*i.e.*, 18, 9, and 0.9 mAh cm^{-2}) with a voltage cutoff condition of 3 V. The current-time profiles are displayed in the top panels of Fig. 1a–c. This harsh condition was set up to prove the feasibility of the reported electrolytes and to facilitate a dramatic comparison between the degradation mechanisms of each cell. Note that the linear sweep voltammetry (Fig. S2.) confirms that the limiting current densities of zinc electrodeposition on Ti foil in the three electrolytes is higher than 5 mA cm^{-2} indicating that the electrodeposition was not controlled by the Zn ion supply. In all the conditions, the voltage profiles in Fig. 1a–c show sharp increases in overpotential within only a few cycles for the 1 m $ZnSO_4$ electrolyte, indicating the possibility of irreversible electrochemical reaction. This result was unexpected because many reports have employed 1 m $ZnSO_4$ electrolyte to demonstrate the electrochemical performances of novel positive electrode materials without noticeable stability issues [34–37,50]. We attribute the reasonable electrochemical properties reported so far to the small areal capacity of the cathode, which corresponds to a minimal fraction of the Zn metal counter electrode (less than 1% per cycle, in most cases). In such cases, the Zn metal would be able to provide sufficient Zn ions to the cathode materials to operate for a few hundred cycles. In stark contrast, the stability of Zn plating/stripping in other electrolytes was much better than that of 1 m $ZnSO_4$. The 1 m $Zn(OTf)_2$ electrolyte exhibited a relatively stable voltage profile; however, the overpotential slowly increased over time, and the fluctuation became more severe when cycled long-term over 1 week (Fig. S3.). However, 5 m AWIS showed a surprisingly stable cycling performance with a negligible change in overpotential under any areal capacity. While the initial overpotential was marginally higher in 5 m AWIS than in 1 m $Zn(OTf)_2$, the overpotential maintained its degree much more consistently in 5 m AWIS, especially during prolonged cycling.

For a more quantitative understanding of electrochemical reversibility, we compared the CEs of the cells in Fig. 1d–f. As expected from the voltage profiles, 5 m AWIS showed a remarkable CE stability, maintaining the value at 100% over hundreds of hours under any areal capacities, including 20 mAh cm^{-2}. For 1 m $ZnSO_4$ electrolyte, the CE value barely marked 100%, which reconciles the impropriety of this electrolyte for rechargeable Zn aqueous batteries. The CE of Zn plating/stripping in 1 m $Zn(OTf)_2$ electrolyte was superior to that in 1 m $ZnSO_4$ electrolyte. The CE of Zn plating/stripping with a 20 mAh cm^{-2} areal capacity marked 100% in the early cycles before it started to fluctuate at the 71st cycle. The general trend of the stability, which is represented by the sudden increase of polarization and voltage variation, arranges the cycle stabilities of Zn plating/stripping in the three electrolytes in a row. To summarize, 5 m AWIS showed the best performance with the stable Zn plating/stripping behavior, and 1 m $ZnSO_4$ showed extreme instability. We noted that with identical salt concentrations, 1 m $Zn(OTf)_2$ showed much better stability than 1 m $ZnSO_4$. This result highlights the critical role of anion species, which affect the solvation structures of electrolytes, in realizing the reversibility of electrochemical deposition and stripping of Zn metal.

To investigate the origin of the different electrochemistry observed in the three electrolytes, we traced the microstructural evolution of Zn deposits and side products during the reaction through *operando* OM. Homemade *in situ* electrochemical cells were designed to contain a Zn foil and a Ti foil in transparent cuvettes (see methods for details and Fig. S1 for the photographs). When cycling the cells, we recorded movie clips using a digital camera equipped in the OM, which are provided with a 200x faster playback speed in Supplementary Information. Movie

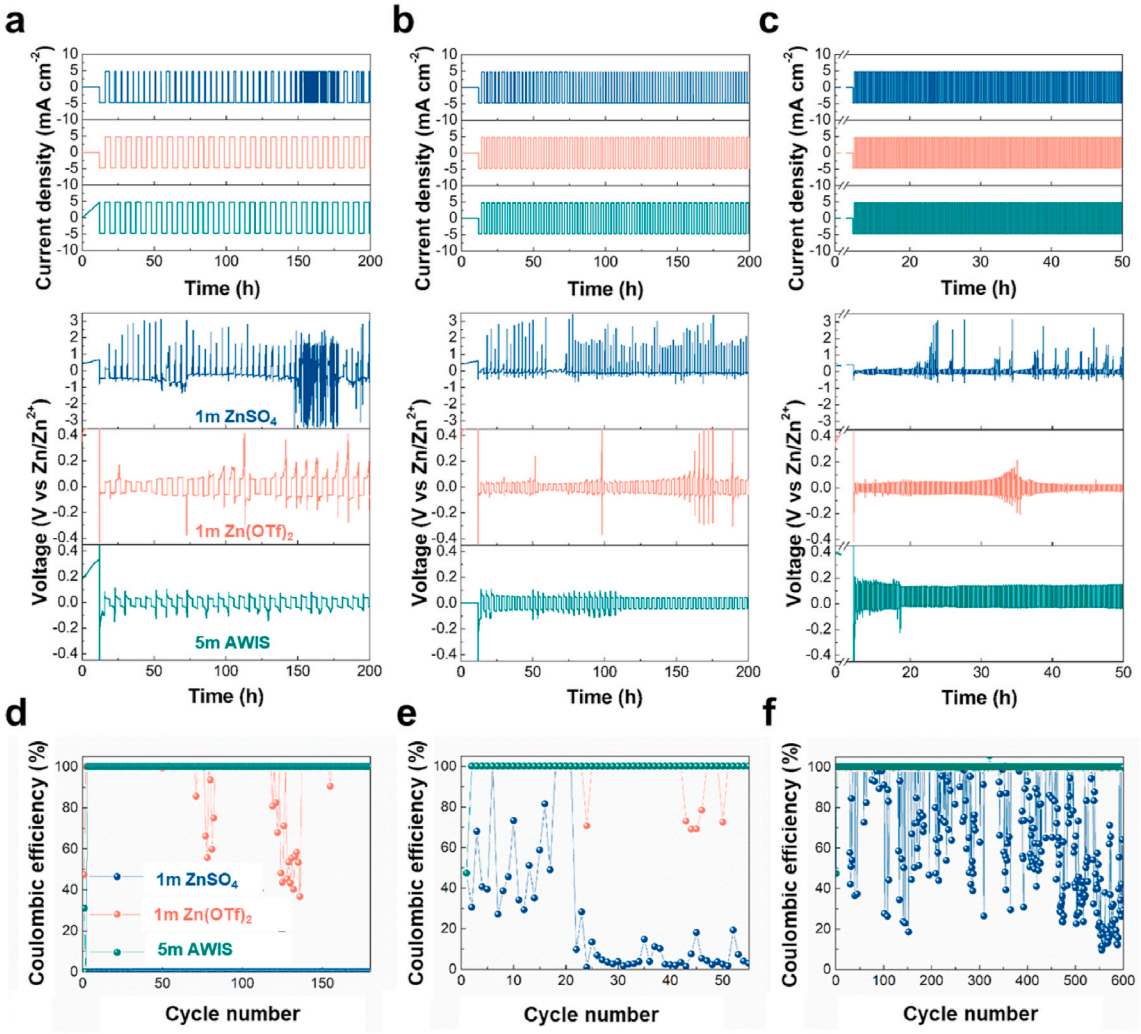

Fig. 1. Zn plating/stripping behavior according to the types of electrolytes in harsh conditions of deep usage of the Zn metal anode. Current density-time (top) and voltage-time curves (bottom) of electrodeposition and stripping of zinc on Ti foil in 1 m $ZnSO_4$ (blue), 1 m $Zn(OTf)_2$ (orange), and 5 m AWIS (green) electrolytes recorded with areal capacities of (a) 20 mAh cm^{-2}, (b) 10 mAh cm^{-2}, and (c) 1 mAh cm^{-2}, and (d-f) corresponding coulombic efficiency as a function of cycle number. The current density was controlled to 5 mA cm^{-2} and each deposition/stripping step was controlled with time unless the voltage reaches the cutoff condition of 3 V. (For interpretation of the references to color in this figure legend, the reader is referred to the Web version of this article.)

snapshots that we captured regularly during the Zn plating/stripping are shown below. The accumulated capacity at the point of capturing is noted on the bottom-right side of each panel. Images that are in the same row show a region within a single electrochemical step of plating or stripping in the designated cycle. After 10 mAh cm^{-2} of Zn was initially deposited on the Ti foil, 90% of the deposited zinc (=9 mAh cm^{-2}) was stripped and plated for the following steps unless the voltage curves reach the 3 V cutoff condition.

Fig. 2 visualizes the microstructural behavior of Zn plating in the 1 m $ZnSO_4$ electrolyte. A white dotted line depicts the boundary of the grown Zn metal on the Ti foil. During the initial plating process, cloud-like Zn metal forms on the surface of the Ti foil, accompanied by a rapid height growth of 200–400 μm at the areal capacity of 10 mAh cm^{-2} (note that the thickness of the Ti foil was 127 μm). In the following stripping process, the volume of the deposited Zn metal initially decreased continuously (the white arrows indicate the direction of shrinkage) following the electrochemical dissolution of Zn into Zn^{2+} ions ($Zn \rightarrow Zn^{2+} + 2e^-$). Interestingly, however, the Zn agglomerates started an unexpected exfoliation from the Ti foil in the middle of the stripping instead of undergoing a gradual dissolution. The local delamination of the Zn deposit exposed the shiny Ti surface. This heterogeneous stripping process is more clearly shown in Supplementary Video SV1 (00:36–00:58). Another interesting point is that hydrogen gas vigorously evolves from the beginning of the stripping process, which forms hydrogen gas bubbles that are marked with red dotted circles in the Figs. We hypothesize that the hydrogen gas evolution originates from the formation of byproducts, such as zinc hydroxide, during the previous reduction process, decreasing the pH value and elevating the hydrogen evolution potential of the electrolyte.

Supplementary video related to this article can be found at https://doi.org/10.1016/j.jpowsour.2020.228334

In the second plating step, the Zn metal preferred to deposit on the exposed Ti surface rather than on the residual Zn agglomerates. This resulted in a smaller morphological change compared to the first electroplating. During the second stripping process, the detachment of the Zn metal cloud occurred again but more completely, as described in the fourth row. We noted that the number of gas bubbles increased as time went on during the second stripping, as shown in Supplementary Video SV1 (01:41–02:13). Figs. 3 and 4 display the precise moments of the physical isolation of the Zn deposit from the Ti foil during the first and second stripping steps, respectively. As shown in the Figs. and the video, once the Zn agglomerates partially delaminate from the Ti foil, exposing a bare surface, the hydrogen evolution reaction accelerates at the interface of the exposed Ti and electrolyte. Thus, hydrogen gas bubbles

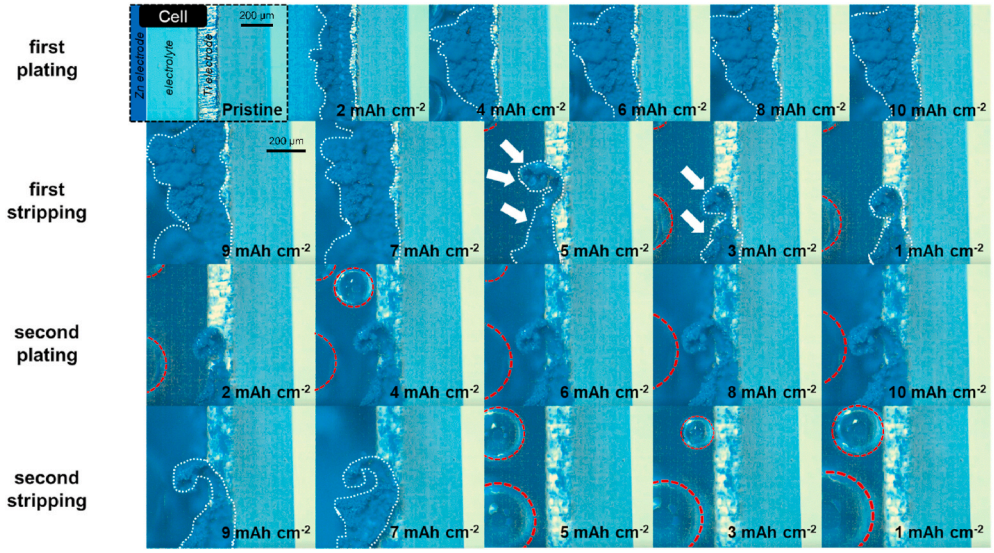

Fig. 2. Observation of the morphologies and microstructural evolution of Zn agglomerates on the Ti foil surface of a Zn||Ti asymmetric cell in 1m $ZnSO_4$ through *operando* OM analysis. Top-left panel shows the cell configuration; accumulated capacity at the point of capturing is noted at the bottom-right side of each paenl; white dotted line shows the boundary of grown Zn metal; red dotted line highlights hydrogen gas bubbles.

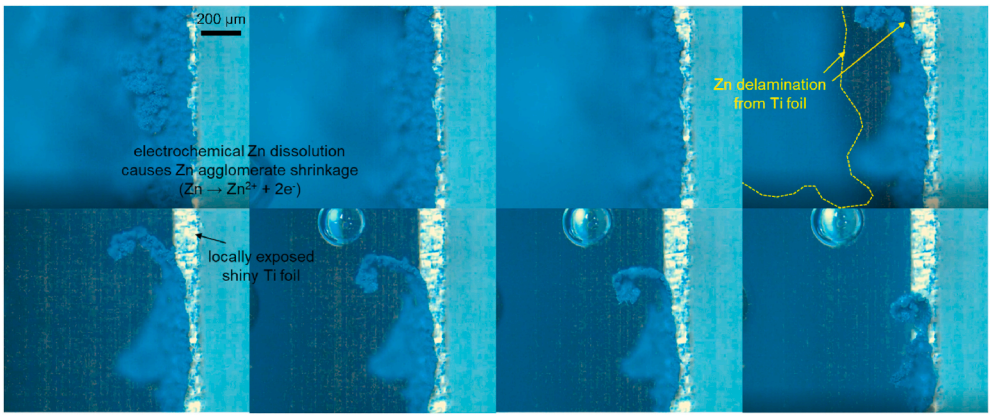

Fig. 3. Visualization of the physical isolation process of the Zn deposit at the first stripping step in 1m $ZnSO_4$. Captured images of the Ti foil surface of a Zn|| Ti asymmetric cell in 1 m $ZnSO_4$ from the *operando* OM analysis.

likely form between the partially detached Zn deposit and the Ti foil, which further facilitates the delamination process. After delamination, the Zn residue still existed heterogeneously on the Ti surface. This finally dissolved into the electrolyte, re-exposing the shiny Ti foil at the end of the second stripping process. However, the hydrogen evolution vigorously occurred until the residual Zn was dissolved, indicating a low coulombic efficiency. The delaminated metal pieces had the possibility of migrating to another side, which could have induced an internal short-circuit or blocked the porous separator membrane, inhibiting the ion diffusion. We therefore attribute the fluctuation observed in the voltage profiles in Fig. 1 to the physical instability of the Zn deposit. The severe deterioration of the microstructures of the Zn deposit and the vigorous hydrogen evolution demonstrated here suggest the impropriety of 1 m $ZnSO_4$ as an electrolyte for Zn aqueous batteries. Investigation of the effect of additives such as $ZnCl_2$ or organic compounds in the zinc sulfate-based electrolytes could be an interesting strategy for improving the stability of Zn anodes in rechargeable aqueous batteries considering the literature in the field of zinc electrowinning [51,52].

As depicted in Fig. 5 and Supplementary Video SV2, the Zn deposition in 1 m $Zn(OTf)_2$ was similar to that of 1 m $ZnSO_4$. However, the Zn cloud in 1 m $Zn(OTf)_2$ consisted of much finer particles, which resulted in denser agglomerates. The Zn cloud grow slower in thickness in the 1 m $Zn(OTf)_2$ electrolyte than in the 1 m $ZnSO_4$ electrolyte. The thickness of the Zn deposit was approximately 150 μm at the end of the first plating (10 mAh cm^{-2}), which is much smaller than that of the 1 m $ZnSO_4$ electrolyte. In the following stripping step, the volume of the deposited Zn metal continuously decreased with only few detachments, which indicates the better physical endurance of the Zn deposit in 1 m $Zn(OTf)_2$. This is consistent with the better electrochemical stability of the 1 m $Zn(OTf)_2$ electrolyte shown in Fig. 1. However, the Zn deposit did not completely dissolve into the electrolyte, and the residual Zn remained on the electrode, so that we observe only a slight change in apparent morphology in the following plating/stripping steps. We hypothesize that this minimal morphological change is due to the faster dissolution of Zn metal near the Ti surface than the top of the Zn deposit, minimizing the change of the outer boundary of the cloudy Zn deposit and generating electrically isolated Zn agglomerates. As the electrochemical cycle repeats, the isolated Zn deposit accumulates and partially falls apart from the Ti surface in the fourth stripping process. We noted that the detachment of the Zn deposit in the 1 m $Zn(OTf)_2$ electrolyte occurred locally and only at a small area fraction of the area of the Ti foil in contrast to the 1 m $ZnSO_4$ electrolyte. The microstructural degradation appeared to be much slower in the latter step, which indicates a stronger adhesion of Zn to the Ti electrode in the 1 m $Zn(OTf)_2$

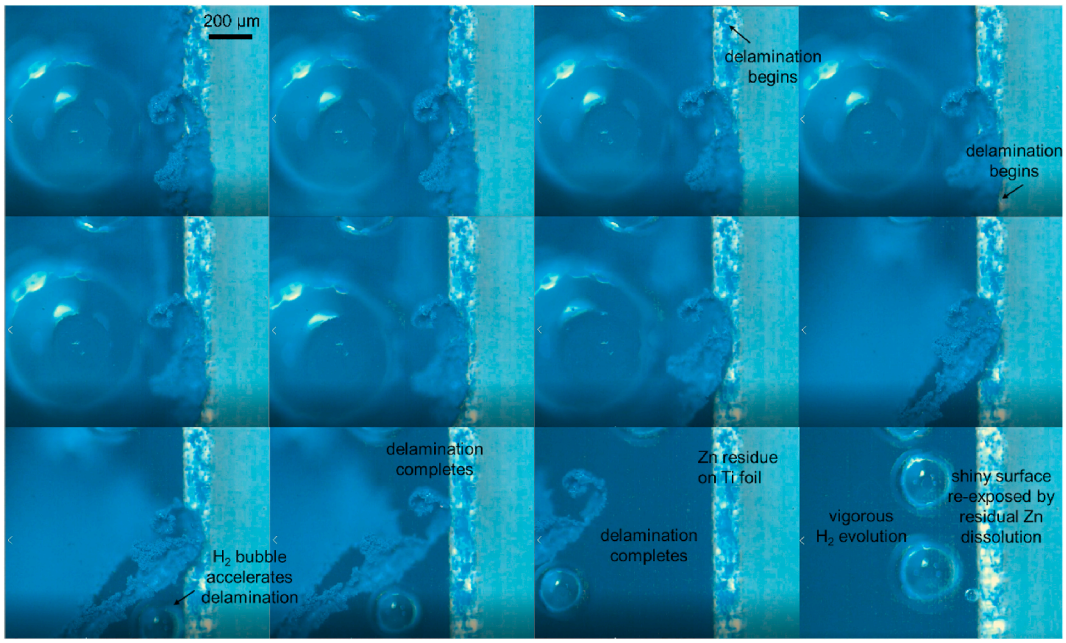

Fig. 4. Visualization of the physical isolation process of the Zn deposit at the second stripping step in 1 m $ZnSO_4$. Captured images of the Ti foil surface of a Zn||Ti asymmetric cell in 1 m $ZnSO_4$ from the *operando* OM analysis.

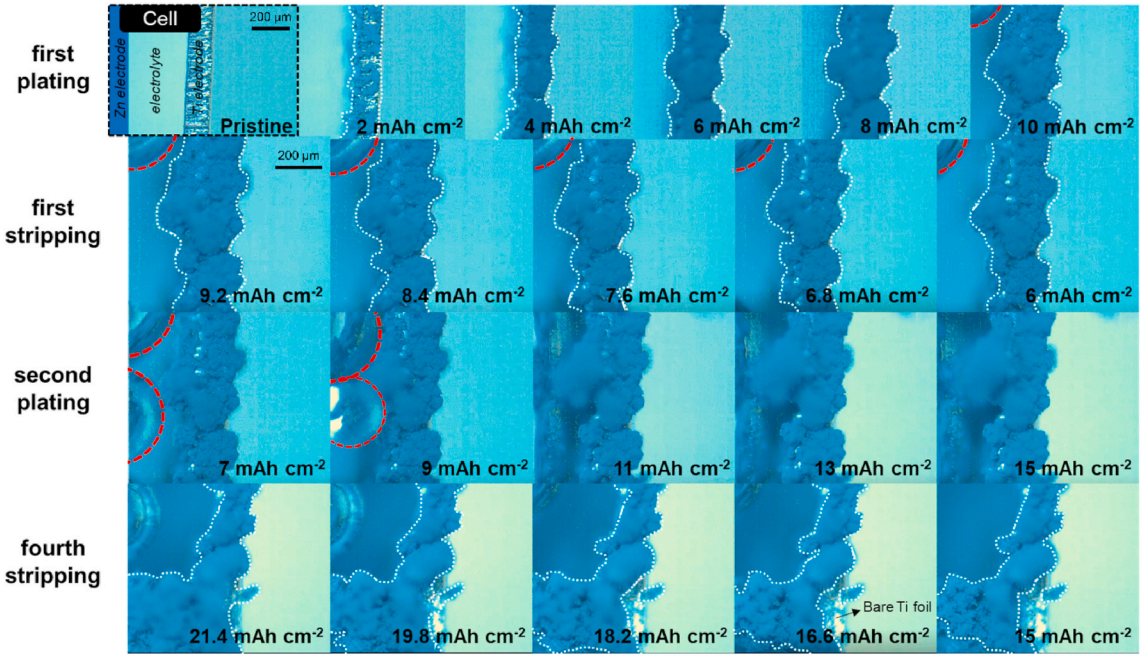

Fig. 5. Observation of the morphologies and microstructural evolution of Zn agglomerates on the Ti foil surface of a Zn||Ti asymmetric cell in 1m Zn $(OTf)_2$ through *operando* OM analysis. Top-left panel shows the cell configuration; accumulated capacity at the point of capturing is noted at the bottom-right side of each paenl; white dotted line shows the boundary of grown Zn metal.

electrolyte. Thus, the larger volume change in $ZnSO_4$ may cause an accelerated microstructural degradation during Zn plating/stripping. This phenomenon may explain why the Zn metal plating/stripping in 1 m $Zn(OTf)_2$ is more stable than it is in 1 m $ZnSO_4$. We will discuss the correlation between the microstructure of the Zn deposit and electrochemistry later. In addition to the partial reversible deposition and dissolution processes, hydrogen gas evolution also occurred in the initial period of the Zn plating/stripping processes (marked with red dotted circles). This evolution was initiated by the formation of solid byproducts, which may cause a decrease in electrochemical reversibility.

Supplementary video related to this article can be found at https://doi.org/10.1016/j.jpowsour.2020.228334

In 5 m AWIS, the Zn deposition exhibited a distinct behavior, as illustrated in Fig. 6 and Supplementary Video SV3. The shiny Ti foil changed to a black color at the very beginning of the electrodeposition process, when the discharge capacity was 0.1 mAh cm^{-2}. This color change was a formation of a highly homogeneous deposit on the Ti foil. Once the black layer formed, it did not completely disappear throughout the electrochemical cycling. Note that no formation of a thin layer was observed in the low-concentration, mildly acidic electrolytes. After the

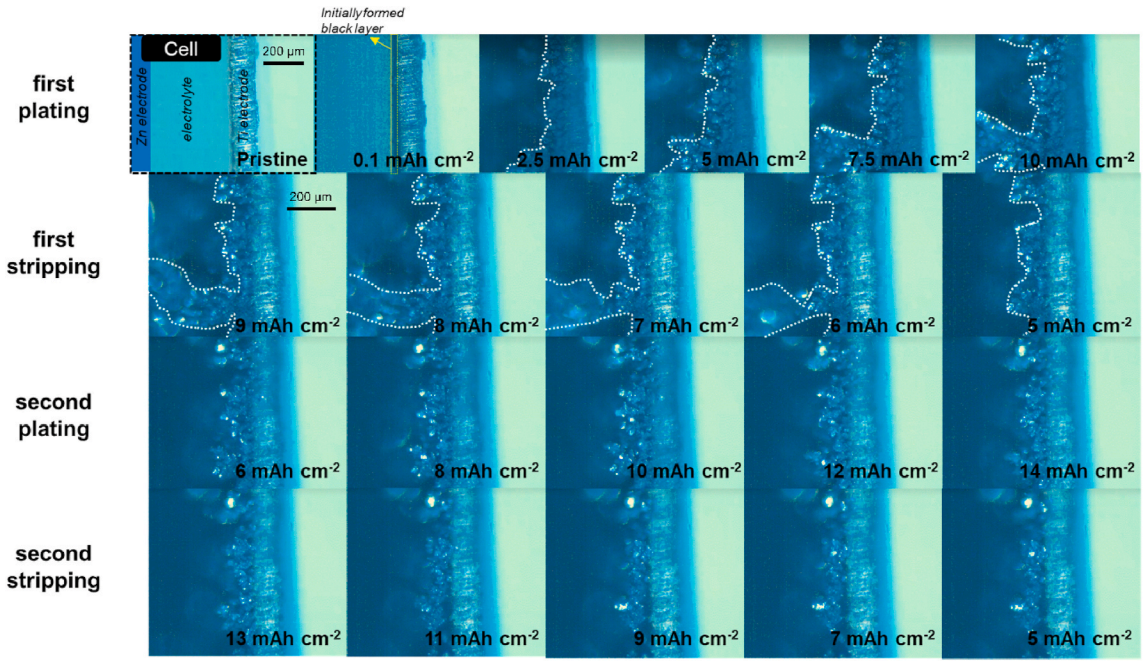

Fig. 6. Observation of the morphologies and microstructural evolution of Zn agglomerates on the Ti foil surface of a Zn||Ti asymmetric cell in 5m AWIS through *operando* OM analysis. Top-left panel shows the cell configuration; accumulated capacity at the point of capturing is noted at the bottom-right side of each paenl; white dotted line shows the boundary of grown Zn metal.

formation of the black layer, the cloudy Zn deposit grew preferentially on the plane side toward the counter Zn electrode, though it grew randomly in the case of diluted electrolytes. We attribute this different growth behavior of the Zn deposit to the initial film formation. As the electroplating continued, glittering metal grew on the formed film during the plating process. This suggests that the primary particles had different morphologies. The grown metal slowly and gradually dissolved into the electrolytes during the stripping process, as represented by a white dotted line. Similar to the 1 m $Zn(OTf)_2$ electrolyte, there was no dramatic microstructural change of the Zn deposit, which indicates the dissolution of Zn from the Ti surface. Delamination did not occur at all in the AWIS electrolyte. The gentle microstructural evolution observed in the 5 m AWIS explains the excellent electrochemical performance of Zn metal.

Supplementary video related to this article can be found at https://doi.org/10.1016/j.jpowsour.2020.228334

To investigate the origin of the stable microstructural and electrochemical behaviors of Zn metal in 5 m AWIS, we focused on two things. First, we used SEM to microscopically study the morphology of the primary Zn particles, the constituents of the cloudy Zn deposit. Second, we used XPS to analyze the chemical structure of the surface passivation layer to understand the nature of the black layer formed in 5 m AWIS.

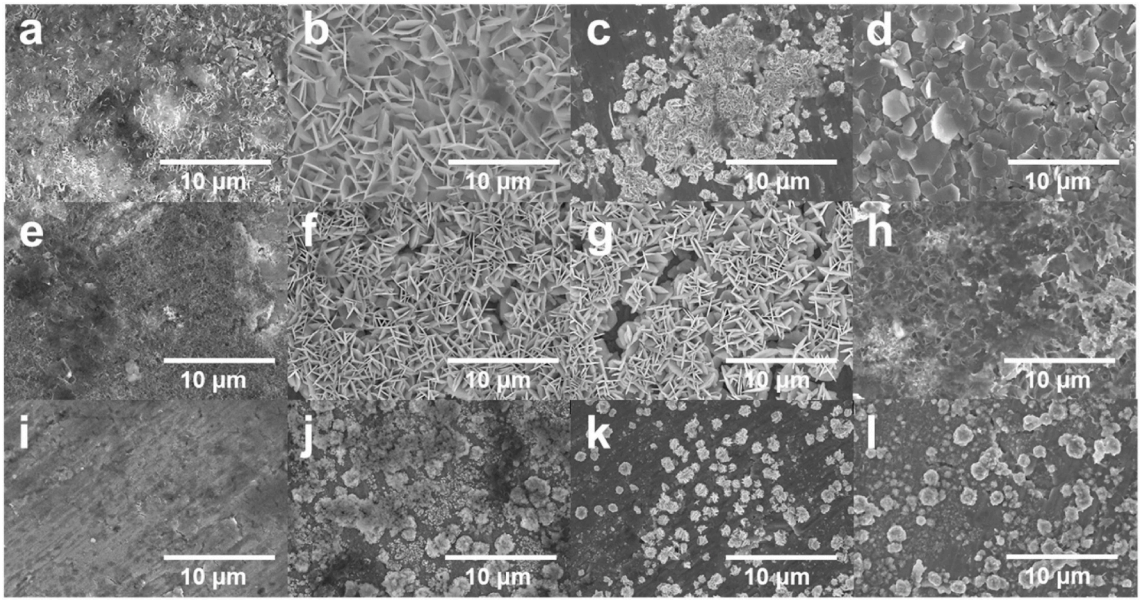

Fig. 7. Surface morphology of the Ti foil surface during the Zn plating/stripping. *Ex situ* SEM images of the Ti electrode at (a, e,i) pristine, (b, f, j) Zn plated for 1 mAh cm^{-2}, (c, g, k) Zn stripped for 0.9 mAh cm^{-2}, and (d, h,i) Zn stripped after long-term cycling in 1 m $ZnSO_4$, 1 m $Zn(OTf)_2$, and 5 m AWIS Zn||Ti asymmetric cells, respectively.

We hypothesize that the different microstructural evolutions according to electrolyte composition are correlated to the SEI layer formation in the initial plating/stripping step.

To observe the microstructural change on a microscopic scale, *ex situ* SEM analysis was performed for electrodes that were retrieved from the cells and disassembled after a rest period, the first plating, the first stripping, and the deterioration, as illustrated in Fig. 7. The electrodes were transferred to an SEM chamber without any exposure to air using an air-free transfer vessel. As shown in Fig. 7a, e, and i, the uncycled Ti electrodes after being immersed in different electrolytes showed a different morphology depending on the electrolyte. The bare Ti electrodes in rested cells with 1 m $ZnSO_4$ and 1 m $Zn(OTf)_2$ had unevenly distributed particles, while the surface of the Ti electrode in the 5 m AWIS was clean. Magnified images of the electrodes that were rested in the diluted electrolytes are shown in Fig. S4. Indeed, a Pourbaix diagram of the Zn confirms the instability of Zn metal in mildly acidic solutions against hydrogen evolution, which is consistent with our results [53]. Therefore, the formed particles on the uncycled Ti electrodes should likely be indexed as chemically produced byproducts, such as zinc oxide, zinc hydroxide, or zinc carbonates [54]. In contrast, 5 m AWIS showed a high compatibility with Zn metal by forming no byproduct. Fig. 7b, f, and j show the deposited Zn at the end of the plating process. Energy-dispersive X-ray spectroscopy (EDS) mapping confirms the Zn element of the deposited Zn (Fig. S5). In the diluted electrolytes, Zn metal grew in the form of hexagonal platelets. However, the Zn particles in 1 m $ZnSO_4$ grew up to 3 μm bigger in diameter compared to those in 1 m $Zn(OTf)_2$. Therefore, the density of the Zn agglomerates is lower in 1 m $ZnSO_4$, which explains the larger volume of the Zn cloudy agglomerate observed in OM. Much finer Zn particles with mossy-like morphology appear in 5 m AWIS, resulting in a highly dense Zn deposit. Fig. S6 shows the magnified image of the mossy-like Zn. We noted in the magnified image that the background of the mossy agglomerate was densely covered with another product that corresponded to the homogeneous black layer observed in OM. The EDS result shown in Fig. S7 reveals that the black layer contained high nitrogen contents. Fig. 7c, g, and k show the electrodes after the first stripping process. As expected from the subtle morphological changes observed in OM, the electrodes cycled in 1 m $Zn(OTf)_2$ and 5 m AWIS showed a negligible change in the SEM images, which only observed the top surface of the electrodes. However, the electrode cycled in the $ZnSO_4$ electrolyte showed a drastic microstructural change after the stripping process. The large platelets disappeared, and the bare Ti foil was exposed as the result of the delamination process.

Based on the SEM analysis, we conclude that the size of the primary Zn particle governs microstructural degradation. The Zn metal grown on Ti electrodes with a large particle size had a sparse structure with fewer physical contacts, and it was easy to be detached from the substrate metal when the volume change became severe. The densely grown Zn particles in 1 m $Zn(OTf)_2$ could endure this for longer cycles while maintaining the microstructures, and the most stable structure with the finest particles in 5 m AWIS could show the best stability of the evolved microstructures during cycling. The SEM images obtained after long-term cycling also support these statements, as shown in Fig. 7d, h, and l. The samples of the Ti electrodes cycled in 1 m $ZnSO_4$ and $Zn(OTf)_2$, which were stopped and retrieved from the cells after the occurrence of sudden polarization, show the destroyed morphology. The surfaces of the electrodes were completely covered with deposits that were different from the Zn platelets observed after initial plating. On the other hand, the sample of the Ti electrode cycled in 5 m AWIS, which was stopped at the same time as the 1 m $Zn(OTf)_2$ cell, showed a marginal difference compared to the electrode after the initial plating.

We further performed *ex situ* XPS analysis to understand the excellent stability of the 5 m AWIS electrolyte by tracing the electrode surface's chemical evolution during the plating/stripping processes in Zn||Ti asymmetric cells. The Zn 2p and S 2p spectra of Ti electrodes at different stages of cycling in 1 m $ZnSO_4$, 1 m $Zn(OTf)_2$, and 5 m AWIS are presented in Fig. 8. The C 1s, O 1s, F 1s, and N 1s spectra are shown in Fig. S8. After being immersed in the electrolytes, peaks are observed in the Zn 2p spectra of all the electrodes (Fig. 8. – top side). The peaks are centered at 1023.5 eV and 1046.5 eV, which correspond to Zn^{2+} in adsorbed salts and byproducts such as zinc hydroxide [16]. The smallest peak width in addition to the silence in the S 2p spectra indicate the main product detected from the electrode rested in 1 m $ZnSO_4$ was zinc hydroxide. This agrees well with the detection of a peak at 531.7 eV in the O 1s spectra (Fig. S8.) [55,56]. In the electrodes immersed in 1 m $Zn(OTf)_2$ and 5 m AWIS, additional peaks were detected in the F 1s and N 1s spectra, corresponding to the electrolyte salts [16,57]. The Ti 2p spectra (Fig. S9.) shows the presence of native oxides at the surface region of Ti foil immersed in both 1 m $ZnSO_4$ and 1 m $Zn(OTf)_2$ electrolytes, which is covered will the adsorbed salt in 5 m AWIS electrolyte.

After the first plating, the intensity of the Zn 2p spectra increased with a new pair of peaks appearing at 1022.3 eV and 1045.2 eV, confirming the plating of metallic Zn (Zn^0) in all the electrolytes [58]. The intensity of the metallic Zn peaks decreased during the first stripping, but did not completely disappear during the following steps indicating the partially reversible electrodeposition/stripping of Zn. On the other hand, salt-related peaks are observed at 169.5 eV, corresponding to the SO_4^{2-} species, in the S 2p spectra of all the electrodes (Fig. 8. – bottom side) [16,23]. This implies the formation of salt-derived byproducts or the SEI layer from the reduction of salt anions. Considering the intensity correlation between the Zn 2p spectra and the S 2p spectra in 1 m $ZnSO_4$ and 1 m $Zn(OTf)_2$ electrolytes, the partially reversible formation/decomposition of the Zn^{2+}- and SO_4^{2-}-containing products is likely accompanied with the electrodeposition and stripping of Zn in those electrolytes. The F 1s spectra in 1 m $Zn(OTf)_2$ also had a specified peak at 689 eV that corresponded to $–CF_3$ bonds, which implied the existence of salt-derived species on the Ti foil surface [16,23,58] which is consistent with the Ti 2p spectra in Fig. S9. Interestingly, 5 m AWIS exhibits the most dynamic evolution of XPS spectra. After the first plating, peaks appeared at 169 eV, 398 eV and 685.5 eV in the S 2p, N 1s, and F 1s spectra, respectively. The peaks are centered at the lower binding energy than the peaks observed in the rested state, suggesting the reduction of $TFSI^-$ anion and the formation of salt-derived byproducts [57]. Surprisingly, the newly observed peaks in the N 1s and F 1s spectra (Fig. S8c.) correspond to lithium nitride, lithium fluoride, and SO_3^{2-}-containing compounds [23,57,59]. Given the fact that we observed the formation of a uniform black layer at the beginning step of the first plating process from the operando OM (Fig. 6.), we concluded that the products of LiTFSI decomposition, *i.e.*, lithium nitride and lithium fluoride, construct a stable and dense passivation layer improving the microstructural and electrochemical stability of 5 m AWIS. In contrast, no solid evidence of the stable SEI layer was found in the XPS spectra of 1 m $ZnSO_4$.

After the first stripping, the intensity of the Zn metal peak in the Zn 2p spectra decreases, confirming the stripping of Zn in all the electrolytes. Interestingly, the intensity of the S 2p spectra relative to other spectra significantly decreases in 1 m $ZnSO_4$ and 1 m $Zn(OTf)_2$, while it maintains strong in 5 m AWIS. We attribute this result to the high instability of the SEl layers in the diluted electrolytes, and the high reversibility of Zn plating/stripping in 5 m AWIS. We noted that the intensities of the peaks corresponding to lithium nitride and lithium fluoride partially decreased, indicating reversible formation and decomposition of the SEI layer during the cycling. Based on the chemical analysis of the cycled electrodes, we conclude that the stability of the formed SEI layer affects the physical endurance of the microstructures, which are highly correlated with the cycle stability. The initially formed black layer in 5 m AWIS was revealed to be a stable passivation film, which offers strong endurance to the Zn deposit against the detachment or deterioration during plating/stripping, even after long-term cycling.

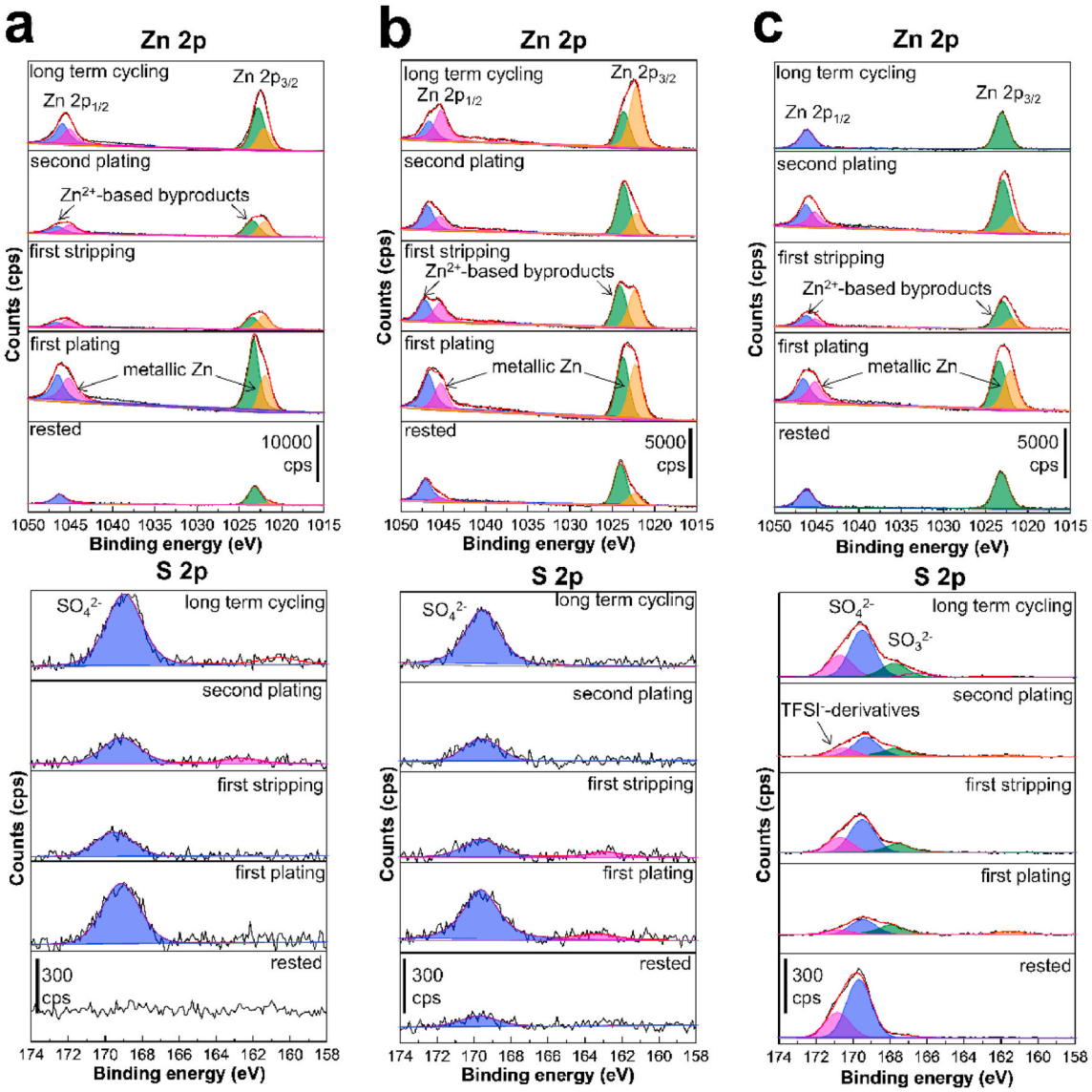

Fig. 8. Chemical investigation of the SEI layer formed on the Ti electrode from rest to long-term cycling. XPS spectra of the Zn 2p and S 2p of the Ti electrode in the (a) $ZnSO_4$, (b) $Zn(OTf)_2$, and (c) AWIS electrolytes during the Zn plating/stripping. In the AWIS electrolyte, it was observed that the $TFSI^-$ anion was reduced to form SEI layer during the first plating.

4. Summary and conclusion

In summary, we investigated the reversibility of Zn metal anodes according to the types of electrolytes (1 m $ZnSO_4$, 1 m $Zn(OTf)_2$, and 5 m AWIS) in the practical condition high areal capacities up to 50 mAh cm^{-2}. Electrochemical tests with harsh conditions of deep discharge/charge processes in the three electrolytes were performed. When considering sudden polarization and voltage variation, 1 m $ZnSO_4$ exhibited a significant instability during electrochemical cycling while the 5 m AWIS showed the best performance with regard to cycle stability. 1 m $Zn(OTf)_2$ exhibited a much longer cycle life than 1 m $ZnSO_4$, even though both are mildly acidic electrolytes with the same molality. We established the correlation between electrochemical properties, microstructures, and chemical environments using *operando* visualization and *ex situ* chemical analysis through OM, SEM, and XPS. The microstructural evolution of primary Zn particles has a large difference with regard to the size and density of distribution. Sparsely grown agglomerates with coarse Zn platelets in the $ZnSO_4$ electrolyte underwent severe delamination from the electrode, which induced an internal short-circuit or inhibited the ion diffusion due to the blocked porous separator membrane. The better cycle stability in the $Zn(OTf)_2$ electrolyte could be explained by the denser agglomerates that were composed of finer Zn platelets, which have a better physical endurance against delamination. In 5 m AWIS, the finest Zn particles formed with a sphere-like shape, while hexagonal platelets of Zn particles grew in the other dilute-concentration electrolytes. Thus, the densest agglomerates with gentle microstructural evolutions were observed, resulting in the excellent cycle performance of the Zn metal anode. We further revealed the existence of the SEI layer and its composition through XPS analysis. The SEI layer formed in 5 m AWIS consisted of fluorinated salts, which in turn enhances the adhesion strength of the Zn deposit to the Ti surface. Therefore, the stable SEI layer in 5 m AWIS improved the reversibility of the Zn metal anode, while the other SEI layers formed in dilute-concentration electrolytes could not act as a stable passivation film. We conclude that the existence of the stable SEI layer, which can help adhere the grown Zn agglomerates to the metal electrode, is a key factor in achieving better cycle stability. This study reveals the correlation between electrolyte composition and capacity degradation through macroscopic- and microscopic-scale support with a chemical analysis. We also emphasize the importance of selecting suitable electrolytes to

enhance the cycle performance of Zn aqueous batteries. In addition, there is further room to investigate the microstructural tuning of Zn metal in the designed electrolytes and the electrochemical protocols to ensure the superb performance of Zn aqueous batteries.

Declaration of competing interest

The authors declare that they have no known competing financial interests or personal relationships that could have appeared to influence the work reported in this paper.

CRediT authorship contribution statement

Sechan Lee: Conceptualization, Writing - original draft, Data curation, Visualization, Investigation. **Inyeong Kang:** Writing - review & editing, Data curation, Visualization, Investigation. **Jihyeon Kim:** Data curation. **So hee Kim:** Resources, Data curation. **Kisuk Kang:** Resources, Supervision, Funding acquisition. **Jihyun Hong:** Conceptualization, Methodology, Writing - review & editing, Supervision, Funding acquisition, Project administration.

Acknowledgement

This work was supported by Korea Institute Science and Technology (No. 2E30201, No. 2V08350), South Korea. This research was also supported by Creative Materials Discovery Program through the National Research Foundation of Korea (NRF) funded by the Ministry of Science, ICT and Future Planning (NRF-2017M3D1A1039553). This work was supported by Project Code (IBS-R006-A2) and the National Research Foundation of Korea (NRF) grant funded by the Korea Government (MSIP) (No. 2018R1A2A1A05079249).

Appendix A. Supplementary data

Supplementary data to this article can be found online at https://doi.org/10.1016/j.jpowsour.2020.228334.

References

[1] F. Wang, O. Borodin, T. Gao, X. Fan, W. Sun, F. Han, A. Faraone, J.A. Dura, K. Xu, C. Wang, Highly reversible zinc metal anode for aqueous batteries, Nat. Mater. 17 (2018) 543–549.
[2] V. Yufit, F. Tariq, D.S. Eastwood, M. Biton, B. Wu, P.D. Lee, N.P. Brandon, Operando visualization and multi-scale tomography studies of dendrite formation and dissolution in zinc batteries, Joule 3 (2019) 485–502.
[3] J. Zhao, J. Zhang, W. Yang, B. Chen, Z. Zhao, H. Qiu, S. Dong, X. Zhou, G. Cui, L. Chen, "Water-in-deep eutectic solvent" electrolytes enable zinc metal anodes for rechargeable aqueous batteries, Nano Energy 57 (2019) 625–634.
[4] Y. Shen, K. Kordesch, The mechanism of capacity fade of rechargeable alkaline manganese dioxide zinc cells, J. Power Sources 87 (2000) 162–166.
[5] K. Fukami, S. Nakanishi, H. Yamasaki, T. Tada, K. Sonoda, N. Kamikawa, N. Tsuji, H. Sakaguchi, Y. Nakato, General mechanism for the synchronization of electrochemical oscillations and self-organized dendrite electrodeposition of metals with ordered 2D and 3D microstructures, J. Phys. Chem. C 111 (2007) 1150–1160.
[6] Y. Ito, M. Nyce, R. Plivelich, M. Klein, D. Steingart, S. Banerjee, Zinc morphology in zinc–nickel flow assisted batteries and impact on performance, J. Power Sources 196 (2011) 2340–2345.
[7] Q. Yang, G. Liang, Y. Guo, Z. Liu, B. Yan, D. Wang, Z. Huang, X. Li, J. Fan, C. Zhi, Do zinc dendrites exist in neutral zinc batteries: a developed electrohealing strategy to in situ rescue in-service batteries, Adv. Mater. 31 (2019) 1903778.
[8] J.M. Bockris, Z. Nagy, A. Damjanovic, On the deposition and dissolution of zinc in alkaline solutions, J. Electrochem. Soc. 119 (1972) 285.
[9] L. Baugh, Corrosion and polarization characteristics of zinc in neutral—acid media—I. Pure zinc in solutions of various sodium salts, Electrochim. Acta 24 (1979) 657–667.
[10] T.K. Hoang, K.E.K. Sun, P. Chen, Corrosion chemistry and protection of zinc & zinc alloys by polymer-containing materials for potential use in rechargeable aqueous batteries, RSC Adv. 5 (2015) 41677–41691.
[11] L.-P. Wang, N.-W. Li, T.-S. Wang, Y.-X. Yin, Y.-G. Guo, C.-R. Wang, Conductive graphite fiber as a stable host for zinc metal anodes, Electrochim. Acta 244 (2017) 172–177.
[12] K. Zhao, C. Wang, Y. Yu, M. Yan, Q. Wei, P. He, Y. Dong, Z. Zhang, X. Wang, L. Mai, Ultrathin surface coating enables stabilized zinc metal anode, Adv. Mater. Interfaces 5 (2018) 1800848.
[13] C. Zhang, J. Holoubek, X. Wu, A. Daniyar, L. Zhu, C. Chen, D.P. Leonard, I. A. Rodríguez-Pérez, J.-X. Jiang, C. Fang, A $ZnCl_2$ water-in-salt electrolyte for a reversible Zn metal anode, Chem. Commun. 54 (2018) 14097–14099.
[14] W. Li, K. Wang, M. Zhou, H. Zhan, S. Cheng, K. Jiang, Advanced low-cost, high-voltage, long-life aqueous hybrid sodium/zinc batteries enabled by a dendrite-free zinc anode and concentrated electrolyte, ACS Appl. Mater. Interfaces 10 (2018) 22059–22066.
[15] C.Y. Chen, K. Matsumoto, K. Kubota, R. Hagiwara, Q. Xu, A room-temperature molten hydrate electrolyte for rechargeable zinc–air batteries, Adv. Energy Mater. 9 (2019) 1900196.
[16] H. Qiu, X. Du, J. Zhao, Y. Wang, J. Ju, Z. Chen, Z. Hu, D. Yan, X. Zhou, G. Cui, Zinc anode-compatible in-situ solid electrolyte interphase via cation solvation modulation, Nat. Commun. 10 (2019) 1–12.
[17] X. Wu, Y. Xu, C. Zhang, D.P. Leonard, A. Markir, J. Lu, X. Ji, Reverse dual-ion battery via a $ZnCl_2$ water-in-salt electrolyte, J. Am. Chem. Soc. 141 (2019) 6338–6344.
[18] J.-D. Xie, J. Patra, P.C. Rath, W.-J. Liu, C.-Y. Su, S.-W. Lee, C.-J. Tseng, Y. A. Gandomi, J.-K. Chang, Highly concentrated carbonate electrolyte for Li-ion batteries with lithium metal and graphite anodes, J. Power Sources 450 (2020) 227657.
[19] K.N. Wood, M. Noked, N.P. Dasgupta, Lithium metal anodes: toward an improved understanding of coupled morphological, electrochemical, and mechanical behavior, ACS Energy Lett. 2 (2017) 664–672.
[20] X. Liu, C. Shen, N. Gao, Q. Hou, F. Song, X. Tian, Y. He, J. Huang, Z. Fang, K. Xie, Concentrated electrolytes based on dual salts of LiFSI and LiODFB for lithium-metal battery, Electrochim. Acta 289 (2018) 422–427.
[21] M. Wang, L. Huai, G. Hu, S. Yang, F. Ren, S. Wang, Z. Zhang, Z. Chen, Z. Peng, C. Shen, Effect of LiFSI concentrations to form thickness-and modulus-controlled SEI layers on lithium metal anodes, J. Phys. Chem. C 122 (2018) 9825–9834.
[22] X. Ren, S. Chen, H. Lee, D. Mei, M.H. Engelhard, S.D. Burton, W. Zhao, J. Zheng, Q. Li, M.S. Ding, Localized high-concentration sulfone electrolytes for high-efficiency lithium-metal batteries, Chem. 4 (2018) 1877–1892.
[23] Y. Gu, W.-W. Wang, Y.-J. Li, Q.-H. Wu, S. Tang, J.-W. Yan, M.-S. Zheng, D.-Y. Wu, C.-H. Fan, W.-Q. Hu, Designable ultra-smooth ultra-thin solid-electrolyte interphases of three alkali metal anodes, Nat. Commun. 9 (2018) 1–9.
[24] R. Rodriguez, K.E. Loeffler, S.S. Nathan, J.K. Sheavly, A. Dolocan, A. Heller, C. B. Mullins, In situ optical imaging of sodium electrodeposition: effects of fluoroethylene carbonate, ACS Energy Lett. 2 (2017) 2051–2057.
[25] X. Zheng, H. Fu, C. Hu, H. Xu, Y. Huang, J. Wen, H. Sun, W. Luo, Y. Huang, Toward a stable sodium metal anode in carbonate electrolyte: a compact, inorganic alloy interface, J. Phys. Chem. Lett. 10 (2019) 707–714.
[26] D. Kundu, B.D. Adams, V. Duffort, S.H. Vajargah, L.F. Nazar, A high-capacity and long-life aqueous rechargeable zinc battery using a metal oxide intercalation cathode, Nat. Energy 1 (2016) 1–8.
[27] H. Pan, Y. Shao, P. Yan, Y. Cheng, K.S. Han, Z. Nie, C. Wang, J. Yang, X. Li, P. Bhattacharya, Reversible aqueous zinc/manganese oxide energy storage from conversion reactions, Nat. Energy 1 (2016) 1–7.
[28] H. Zhang, J. Wang, Q. Liu, W. He, Z. Lai, X. Zhang, M. Yu, Y. Tong, X. Lu, Extracting oxygen anions from $ZnMn_2O_4$: robust cathode for flexible all-solid-state Zn-ion batteries, Energy Storage Mater. 21 (2019) 154–161.
[29] C. Zhu, G. Fang, S. Liang, Z. Chen, Z. Wang, J. Ma, H. Wang, B. Tang, X. Zheng, J. Zhou, Electrochemically induced cationic defect in MnO intercalation cathode for aqueous zinc-ion battery, Energy Storage Mater. 24 (2020) 394–401.
[30] M. Sun, D.S. Li, Y.F. Wang, W.L. Liu, M.M. Ren, F.G. Kong, S.J. Wang, Y.Z. Guo, Y. M. Liu, Mn_3O_4@ NC composite nanorods as a cathode for rechargeable aqueous Zn-ion batteries, ChemElectroChem 6 (2019) 2510–2516.
[31] J. Shin, J. Lee, Y. Park, J.W. Choi, Aqueous zinc ion batteries: focus on zinc metal anodes, Chem. Sci. 11 (2020) 2028–2044.
[32] Z. Zhao, J. Zhao, Z. Hu, J. Li, J. Li, Y. Zhang, C. Wang, G. Cui, Long-life and deeply rechargeable aqueous Zn anodes enabled by a multifunctional brightener-inspired interphase, Energy Environ. Sci. 12 (2019) 1938–1949.
[33] Q. Zhang, J. Luan, L. Fu, S. Wu, Y. Tang, X. Ji, H. Wang, The three-dimensional dendrite-free zinc anode on a copper mesh with a zinc-oriented polyacrylamide electrolyte additive, Angew. Chem. Int. Ed. 58 (2019) 15841–15847.
[34] S. Islam, M.H. Alfaruqi, J. Song, S. Kim, D.T. Pham, J. Jo, S. Kim, V. Mathew, J. P. Baboo, Z. Xiu, Carbon-coated manganese dioxide nanoparticles and their enhanced electrochemical properties for zinc-ion battery applications, J. Energy Chem. 26 (2017) 815–819.
[35] M.H. Alfaruqi, S. Islam, D.Y. Putro, V. Mathew, S. Kim, J. Jo, S. Kim, Y.-K. Sun, K. Kim, J. Kim, Structural transformation and electrochemical study of layered MnO_2 in rechargeable aqueous zinc-ion battery, Electrochim. Acta 276 (2018) 1–11.
[36] M.H. Alfaruqi, S. Islam, V. Mathew, J. Song, S. Kim, D.P. Tung, J. Jo, S. Kim, J. P. Baboo, Z. Xiu, Ambient redox synthesis of vanadium-doped manganese dioxide nanoparticles and their enhanced zinc storage properties, Appl. Surf. Sci. 404 (2017) 435–442.
[37] M.H. Alfaruqi, V. Mathew, J. Song, S. Kim, S. Islam, D.T. Pham, J. Jo, S. Kim, J. P. Baboo, Z. Xiu, Electrochemical zinc intercalation in lithium vanadium oxide: a high-capacity zinc-ion battery cathode, Chem. Mater. 29 (2017) 1684–1694.
[38] H. Qin, Z. Yang, L. Chen, X. Chen, L. Wang, A high-rate aqueous rechargeable zinc ion battery based on the VS_4@ rGO nanocomposite, J. Mater. Chem. 6 (2018) 23757–23765.
[39] D. Kundu, P. Oberholzer, C. Glaros, A. Bouzid, E. Tervoort, A. Pasquarello, M. Niederberger, Organic cathode for aqueous Zn-ion batteries: taming a unique phase evolution toward stable electrochemical cycling, Chem. Mater. 30 (2018) 3874–3881.

[40] F. Wan, L. Zhang, X. Wang, S. Bi, Z. Niu, J. Chen, An aqueous rechargeable zinc-organic battery with hybrid mechanism, Adv. Funct. Mater. 28 (2018) 1804975.
[41] Q. Dou, S. Lei, D.-W. Wang, Q. Zhang, D. Xiao, H. Guo, A. Wang, H. Yang, Y. Li, S. Shi, Safe and high-rate supercapacitors based on an "acetonitrile/water in salt" hybrid electrolyte, Energy Environ. Sci. 11 (2018) 3212–3219.
[42] N. Zhang, F. Cheng, Y. Liu, Q. Zhao, K. Lei, C. Chen, X. Liu, J. Chen, Cation-deficient spinel $ZnMn_2O_4$ cathode in Zn $(CF_3SO_3)_2$ electrolyte for rechargeable aqueous Zn-ion battery, J. Am. Chem. Soc. 138 (2016) 12894–12901.
[43] N. Zhang, F. Cheng, J. Liu, L. Wang, X. Long, X. Liu, F. Li, J. Chen, Rechargeable aqueous zinc-manganese dioxide batteries with high energy and power densities, Nat. Commun. 8 (2017) 1–9.
[44] N. Zhang, Y. Dong, M. Jia, X. Bian, Y. Wang, M. Qiu, J. Xu, Y. Liu, L. Jiao, F. Cheng, Rechargeable aqueous $Zn–V_2O_5$ battery with high energy density and long cycle life, ACS Energy Lett. 3 (2018) 1366–1372.
[45] Q. Zhao, W. Huang, Z. Luo, L. Liu, Y. Lu, Y. Li, L. Li, J. Hu, H. Ma, J. Chen, High-capacity aqueous zinc batteries using sustainable quinone electrodes, Sci. Adv. 4 (2018), eaao1761.
[46] S. Zhao, B. Han, D. Zhang, Q. Huang, L. Xiao, L. Chen, D.G. Ivey, Y. Deng, W. Wei, Unravelling the reaction chemistry and degradation mechanism in aqueous Zn/MnO_2 rechargeable batteries, J. Mater. Chem. A 6 (2018) 5733–5739.
[47] H. Glatz, E. Tervoort, D. Kundu, Unveiling critical insight into the Zn metal anode cyclability in mildly acidic aqueous electrolytes: implications for aqueous zinc batteries, ACS Appl. Mater. Interfaces 12 (2019) 3522–3530.
[48] L. Wang, Y. Zhang, H. Hu, H.-Y. Shi, Y. Song, D. Guo, X.-X. Liu, X. Sun, A $Zn(ClO_4)_2$ electrolyte enabling long-life zinc metal electrodes for rechargeable aqueous zinc batteries, ACS Appl. Mater. Interfaces 11 (2019) 42000–42005.
[49] S. Chen, R. Lan, J. Humphreys, S. Tao, Perchlorate based 'over-saturated gel electrolyte'for an aqueous rechargeable hybrid Zn-Li battery, ACS Appl. Energy Mater. 3 (2020) 2526–2536.
[50] H. Li, Z. Liu, G. Liang, Y. Huang, Y. Huang, M. Zhu, Z. Pei, Q. Xue, Z. Tang, Y. Wang, Waterproof and tailorable elastic rechargeable yarn zinc ion batteries by a cross-linked polyacrylamide electrolyte, ACS Nano 12 (2018) 3140–3148.
[51] G. Trejo, Y. Meas, P. Ozil, E. Chainet, B. Nguyen, Nucleation and growth of zinc from chloride concentrated solutions, J. Electrochem. Soc. 145 (1998) 4090–4097.
[52] D. Baik, D. Fray, Electrodeposition of zinc from high acid zinc chloride solutions, J. Appl. Electrochem. 31 (2001) 1141–1147.
[53] S. Thomas, N. Birbilis, M. Venkatraman, I. Cole, Corrosion of zinc as a function of pH, Corrosion 68 (2012), 015009-015001-1-5009-0150-9.
[54] F. Wan, L. Zhang, X. Dai, X. Wang, Z. Niu, J. Chen, Aqueous rechargeable zinc/sodium vanadate batteries with enhanced performance from simultaneous insertion of dual carriers, Nat. Commun. 9 (2018) 1–11.
[55] C.-H. Huang, Y.-L. Jan, W.-J. Chuang, P.-T. Lu, Investigation of approaches to control the compositions of Zn (Se, OH) buffers prepared by chemical bath deposition process for Cu (In, Ga) Se2 (CIGS) solar cells, Crystals 8 (2018) 343.
[56] R. Al-Gaashani, S. Radiman, A. Daud, N. Tabet, Y. Al-Douri, XPS and optical studies of different morphologies of ZnO nanostructures prepared by microwave methods, Ceram. Int. 39 (2013) 2283–2292.
[57] C. Xu, B. Sun, T. Gustafsson, K. Edström, D. Brandell, M. Hahlin, Interface layer formation in solid polymer electrolyte lithium batteries: an XPS study, J. Mater. Chem. A 2 (2014) 7256–7264.
[58] G. Tian, Z. Zhao, A. Sarapulova, C. Das, L. Zhu, S. Liu, A. Missiul, E. Welter, J. Maibach, S. Dsoke, Understanding the Li-ion storage mechanism in a carbon composited zinc sulfide electrode, J. Mater. Chem. A 7 (2019) 15640–15653.
[59] V. Nilsson, R. Younesi, D. Brandell, K. Edström, P. Johansson, Critical evaluation of the stability of highly concentrated LiTFSI-Acetonitrile electrolytes vs. graphite, lithium metal and LiFePO4 electrodes, J. Power Sources 384 (2018) 334–341.